

Article

Frequency Conversion Interface towards Quantum Network: From Atomic Transition Line to Fiber Optical Communication Band

Shujing Li ^{1,2}, Jiaxin Bao ^{1,2}, Qiqi Deng ^{1,2}, Lirong Chen ^{1,2} and Hai Wang ^{1,2,*}

¹ State Key Laboratory of Quantum Optics and Quantum Optics Devices, Institute of Opto-Electronics, Shanxi University, Taiyuan 030006, China; lishujing@sxu.edu.cn (S.L.); jiaxinbao96@163.com (J.B.); 18435207477@163.com (Q.D.); clr@sxu.edu.cn (L.C.)

² Collaborative Innovation Center of Extreme Optics, Shanxi University, Taiyuan 030006, China

* Correspondence: wanghai@sxu.edu.cn

Abstract: Quantum repeater is a key component of quantum network, and atomic memory is one of the important candidates for constructing quantum repeater. However, the atomic transition wavelength is not suitable for long-distance transmission in optical fiber. To bridge atomic memory and fiber communication, we demonstrate a frequency conversion interface from rubidium D1 line (795 nm) to the optical communication L-band (1621 nm) based on difference frequency generation. To reduce broadband noise of spontaneous Raman scattering caused by strong pumping light, we use a combination of two cascaded etalons and a Fabry-Perot cavity with low finesse to narrow the noise bandwidth to 11.7 MHz. The filtering system is built by common optical elements and is easy to use; it can be widely applied in frequency conversion process. We show that the signal-noise ratio of the converted field is good enough to reduce the input photon number below 1 under the condition of low external device conversion efficiency (0.51%) and large duration of input pulse (250 ns). The demonstrated frequency conversion interface has important potential application in quantum networks.

Keywords: quantum network; frequency conversion interface; difference frequency generation; optical communication band



Citation: Li, S.; Bao, J.; Deng, Q.; Chen, L.; Wang, H. Frequency Conversion Interface towards Quantum Network: From Atomic Transition Line to Fiber Optical Communication Band. *Appl. Sci.* **2022**, *12*, 6522. <https://doi.org/10.3390/app12136522>

Academic Editors: Nuno Silva and Habib Hamam

Received: 4 June 2022

Accepted: 25 June 2022

Published: 27 June 2022

Publisher's Note: MDPI stays neutral with regard to jurisdictional claims in published maps and institutional affiliations.



Copyright: © 2022 by the authors. Licensee MDPI, Basel, Switzerland. This article is an open access article distributed under the terms and conditions of the Creative Commons Attribution (CC BY) license (<https://creativecommons.org/licenses/by/4.0/>).

1. Introduction

The core task of quantum communication is to realize remote transmission of quantum information [1,2]. However, direct transmission of quantum information over long distance (>1000 km) in optical fiber network is intractable because of exponential loss of the transmitted photons. To solve this problem, the concept of quantum repeater is proposed, in which quantum storage plays a key role [3–5]. Atomic ensemble [6,7], single atom [8,9], trapped ions [10,11] and solid-state systems [12,13] are all potential candidates for quantum repeater, in which quantum storage has been actively performed. However, the photons emitted from these systems are in the visible to near infrared range, where the loss in optical fiber is significant. Therefore, it is a basic requirement of long-distance quantum communication to transform the emitted photons into communication band [14–17]. The frequency conversion from storage band to communication band also provides the foundation for the construction of heterogeneous quantum network, in which network nodes are served by different storage mediums. One can take advantage of various capabilities offered by diversity of quantum nodes [18,19].

The difference frequency generation (DFG) in nonlinear crystal is often used for frequency down conversion [20–24]. In recent years, it is a very attractive research field to convert light field from storage band to communication band by using DFG. The combination of emissive quantum memory and frequency conversion with DFG is the most

promising scheme for building quantum repeater [25–28]. The frequency conversion to communication band has been demonstrated from different wavelengths resonant with various storage mediums, including atoms [15,29], ions [30,31], quantum dot [16], nitrogen-vacancy centers [32,33], etc.

Rubidium (Rb) atom is usually used for quantum storage. Great progress has been made in the field of photon-atom entanglement quantum interface based on Rb atomic ensemble [6,14,34–38]. Most of them work at 795 nm which corresponds to the transition of ^{87}Rb D1 line, because the transition line has a concise energy level structure which can realize clean and effective manipulation of atomic internal states. However, there are few experimental reports on frequency conversion from 795 nm to communication band [14,28]. Using four-wave mixing in cold atoms with large optical thickness, A. G. Radnaev et al., achieved the conversion of 795 nm to the communication O-band 1367 nm [14], however, the target wavelength of the conversion is strictly dependent on the atomic energy level. Yong Yu et al., converted the 795 nm light to the O-band 1342 nm by using DFG in periodically poled lithium niobate (PPLN) waveguide [28]. So far, there is no experimental report on the conversion from 795 nm to C-band or L-band. By using pumping light at 1620 nm, the 795 nm photons can be converted to C-band 1561 nm. However, the commercial amplifier at 1620 nm is expensive, and its output power is relatively low.

In this paper, we report the first experimental study to convert light field from 795 nm to L-band 1621 nm by using DFG in PPLN waveguide. The transmission loss of L-band in fiber channel (0.18 dB/km) is lower than that of O-band (0.3 dB/km), which will significantly improve the successful probability of long-distance entanglement distribution [4,39]. L-band is also the mainstream choice for expanding communication bandwidth at present due to low transmission loss [40,41]. In DFG process, the strong pumping beam causes spontaneous Raman scattering (SRS) noise, which typically covers over a region of several hundreds of nanometers. The noise suppression is important for improving the signal-noise ratio (SNR) of the converted field, especially for the frequency conversion of quantum state light field [15,22,42–44].

To suppress the broadband noise, we design a three-stage filtering system to compress the noise bandwidth to 11.7 MHz, which is slightly larger than the natural line width 6 MHz. In our filtering scheme, a band-pass filter and a fiber Bragg grating (FBG) are used to limit the noise range to 1 nm. Then, the noise bandwidth is further narrowed to 11.7 MHz by combining two cascaded etalons with different lengths and a confocal Fabry-Perot (F-P) cavity with a finesse of 28.7. The cascaded etalons and F-P cavity reduces the noise level by three orders of magnitude. As far as we know, this bandwidth of filtering system is the narrowest in experimental reports of frequency conversion. The optical components included in our filtering system are easy to use, which can be widely used in frequency conversion process. Based on the strong noise suppression, we show that the SNR of converted field is good enough to reduce the input photon number below 1 under the condition of low external device conversion efficiency (0.51%) and large duration of input pulse (250 ns). This work is a meaningful attempt to realize the frequency conversion interface between quantum memory at ^{87}Rb D1 line and communication band, which enriches the toolbox of fiber quantum networks.

2. Experimental Setup

The experimental setup is shown in Figure 1. The 795 nm input light comes from an external cavity diode laser (ECDL). Its frequency is locked to the saturated absorption line of rubidium atom. A seed laser beam from another ECDL at 1560 nm is amplified by an Erbium-doped fiber amplifier, and then it is used as the pumping field for the DFG. The frequency of the 1560 nm ECDL is stabilized by locking it to a reference cavity made of ultra-low expansion (ULE) glass. A band-pass filter BF1 centered at 1560 nm with a bandwidth of 12 nm is used to reduce the amplified spontaneous emission noise generated by the amplifier. The light pulse at 795 nm is produced by an acousto-optic modulator AOM1 (Gooch & Housego 3200-124, rise time 15 ns) which is arranged in double passage

configuration. AOM1 is driven by an RF source (MODA200-B4-33). The output power of the RF source can be modulated by external analog signal, which drives AOM1 to generate analog light pulse. This configuration allows the generation of Gaussian light pulses with a FWHM of 30 ns.

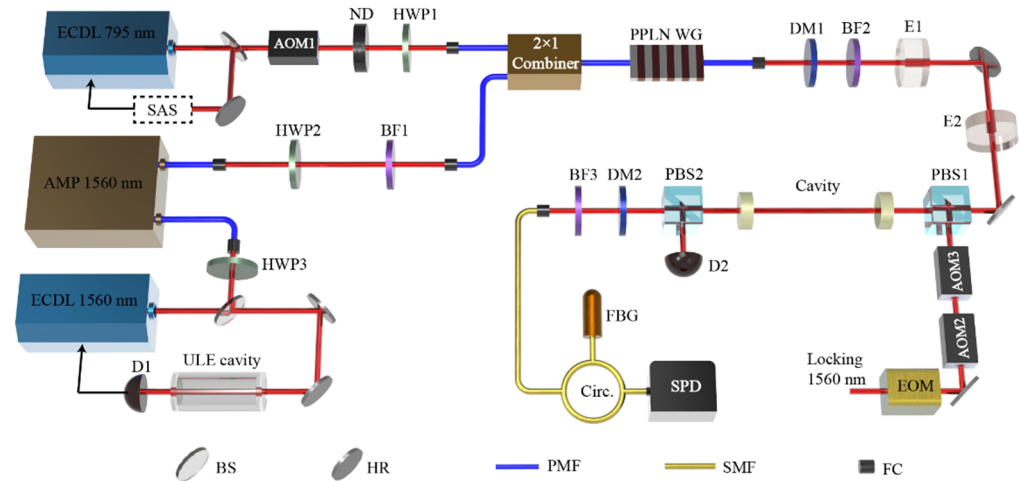


Figure 1. Experimental setup for frequency down conversion. ECDL: external cavity diode laser. AMP: fiber amplifier. SAS: saturated absorption spectroscopy. AOM1-3: acousto-optic modulators. ND: neutral density filter. HWP: half waveplate. BF1-3: band-pass filters. DM1-2: dichroic mirrors. E1-2: etalons. PBS1-2: polarization beam splitters. Circ.: fiber circulator. FBG: fiber Bragg grating. SPD: single photon detector. EOM: electro-optic modulator. D1-2: photodetectors. BS: beam splitter. HR: high reflectivity mirror. PMF: polarization-maintaining fiber. SMF: single mode fiber. FC: fiber collimator.

A set of neutral density filters are employed to acquire the light pulse containing several photons. The total transmittance of the set of neutral density filters $T_{att} = 4.3 \times 10^{-6}$. The power distribution of Gaussian pulse generated by AOM1 can be expressed as $f(t) = A \text{Exp}[-\frac{4 \ln 2}{\Delta_{FWHM}^2} t^2]$, where A is the peak power, Δ_{FWHM} is the FWHM of light pulse. After the set of neutral density filters, the power distribution of light pulse is attenuated to $T_{att} f(t)$. By integrating the power distribution, we can obtain the energy contained in the pulse $\frac{AT_{att}\Delta_{FWHM}}{2} \sqrt{\frac{\pi}{\ln 2}}$. The average photon number contained in the pulse $\mu_{in} = \frac{AT_{att}\Delta_{FWHM}}{2\hbar\nu} \sqrt{\frac{\pi}{\ln 2}}$, where $\hbar\nu$ is the energy of a photon, and ν is the photon frequency corresponding to 795 nm. For a fixed Δ_{FWHM} , A specific μ_{in} can be obtained by adjusting the peak power of light pulse.

We use a fiber-coupled PPLN waveguide module (HP Photonics) for DFG process, which includes a 2×1 combiner and a waveguide module. The input light at 795 nm and the pumping light at 1560 nm are set to vertical polarization by half wave-plates HWP1 and HWP2, respectively, and then are guided to the 2×1 combiner through polarization-maintaining fibers (PMF). The 2×1 combiner couples the two light beams into a single output fiber which is fused to the input of the waveguide. The transmission of the 2×1 combiner for 795 nm and 1560 nm beams are 67% and 60%, respectively. The input coupling efficiency of the waveguide is 55% for both beams. The waveguide is 19 mm long and heated to 58 °C to produce effective nonlinear process. The 1621 nm converted light from the waveguide is outputted through a PMF with coupling efficiency of 65%.

For quantum frequency conversion, the converted field at 1621 nm needs to be isolated from the noise. The noise of the down-conversion process mainly comes from: leakage of the strong pumping light at 1560 nm, non-converted 795 nm input field, SRS noise by strong pump, and a light at 780 nm created by weakly phase matched second harmonic generation (SHG) of the strong pump. After the waveguide module, a dichroic mirror DM1 (82% transmission) is used to remove the leaked 1560 nm pumping light, which suppresses

the pumping light by >25 dB. To block the non-converted input light at 795 nm and the light at 780 nm created by SHG, we use a band-pass filter BF2 (72% transmission, bandwidth of 12 nm), its optical density is ~6 in the wavelength range of 780–795 nm.

The SRS noise typically covers over a region of several hundreds of nanometers, which seriously degrades the fidelity of quantum frequency conversion [23]. We design a three-stage filtering system to reduce the noise level by narrowing its bandwidth. After BF2 the converted light passes through two etalons E1 and E2, a F-P cavity and a FBG in turn. The FBG (1 nm bandwidth) works together with a fiber circulator, as shown in Figure 1. The BF2 and FBG form the first-stage filter, in which BF2 narrows the noise bandwidth to 12 nm, and FBG further narrows it to 1 nm. Considering the coupling efficiency of the input fiber and the insertion loss of the circulator, the measured whole efficiency of FBG is 0.43, that is, the ratio of output power of the circulator to the input power in front of the input fiber collimator. The efficiency of the first-stage filter is 31%, which is the product of the transmission of BF2 and FBG.

The second-stage filter consists of the two etalons E1 and E2 with finesse of 30. E1 and E2, made of fused quartz with refractive index of 1.44, are 11.7 mm and 4.3 mm long, respectively. For E1 (E2), the free spectral range is 8.9 GHz (24.2 GHz) and the measured linewidth is 284 MHz (770 MHz). They are both resonant with the down-converted light field by adjusting their temperatures. Figure 2a shows the theoretical transmission spectra of E1 and E2 as a function of the frequency detuning from down-converted field. In the wavelength range of 1 nm which corresponds to the frequency detuning from –55 GHz to 55 GHz, their transmission peaks only coincide at the converted frequency, while other transmission peaks are all staggered. The spectral function of the second-stage filter depends on the product of the transmission spectra of E1 and E2, as shown by the green solid line in Figure 2a. It is obvious that the noise is suppressed at all frequencies except for a narrow region centered at the converted frequency. After the first- and second-stage filters, the noise bandwidth (FWHM) is narrowed to 254 MHz. The transmission of a single etalon is 0.92, and the efficiency of the second-stage filter is 0.84.

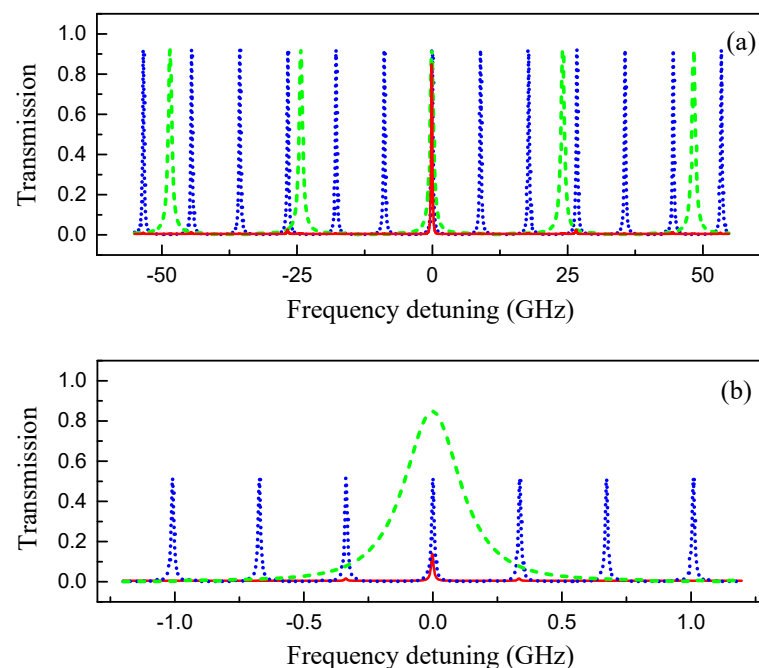


Figure 2. (a) The theoretical transmission spectrum of etalons E1 (blue dotted) and E2 (green dash). The red solid line represents the spectral function of the second-stage filter. (b) The spectral function of the F-P cavity (blue dotted) and the second-stage filter (green dash). The red solid line represents the spectral function of the three-stage filtering system.

The third-stage filter is the confocal F-P cavity with standing wave configuration. Its free spectral range and linewidth are measured to be 336 MHz and 11.7 MHz, respectively. Therefore, the finesse of the cavity is 28.7. A locking beam at 1560 nm is injected into the F-P cavity from polarization beam splitter PBS1 to lock the cavity length to be resonant with the converted frequency. The 1560 nm locking light and the pumping light are derived from the same ECDL master oscillator. We use an electro-optic modulator (EOM) to produce phase-modulation sidebands and lock the cavity by Pound-Drever-Hall technology [45]. The transmitted locking beam from the cavity is steered to detector D2 by PBS2. To make sure that the cavity resonates with the 1621 nm converted light and the 1560 nm locking beam at the same time, two acousto-optic modulators AOM2 and AOM3 are employed to adjust the frequency of the locking beam. Figure 2b shows the transmission spectra of the F-P cavity (blue dotted line) and the second-stage filter (red dashed line). The spectral function of the three-stage filtering system is determined by the product of the transmission spectra of the cavity, the second-stage filter and the first-stage filter, shown by the green solid line in Figure 2b. From the above analysis, we can see that this hierarchical filtering system compresses the broadband SRS noise to a single longitudinal mode output of the narrow-band F-P cavity. The linewidth of the three-stage filtering system is approximately equal to that of the F-P cavity.

Under locking state, the transmission of the converted light through the F-P cavity is 0.76. To prevent the residual locking light from entering the detection path of the converted field, a dichroic mirror DM2 (94% transmission) and a band-pass filter BF3 (72% transmission) are placed after the F-P cavity to block it. Accounting for these losses introduced by DM2 and BF3, the efficiency of the third-stage filter is 0.51. The efficiency of the three-stage filtering system is 0.13, which is the product of the first-, second-, and third-stage filters. In addition to the three-stage filtering system, the dichroic mirror DM1 is used behind the PPLN module to filter the pumping field. Therefore, the efficiency of the whole filtering system is 0.11. The converted photons are detected by a fiber-coupled single photon detector SPD (ID230, ID Quantique). The SPD works in free running state, and its detection efficiency and dead time is set to 0.2 and 20 μ s, respectively. Under this setting, the dark count rate is about 250/s. The output data of the SPD are acquired and analyzed by a field programmable gate array (FPGA).

3. Influence on Noise Suppression and Pulse Shape by Filtering System

We measure the noise suppression by the filtering system. When the pump light was blocked and only a light pulse at 795 nm is incident into the frequency conversion module, the noise level of the leaked 795 nm field can be measured after the filtering system. The 795 nm input pulse contains 50 photons with a FWHM of 100 ns. The measurement window is 640 ns which is centered on the pulse peak. By repeating the noise collection with FPGA (repeat time of 1.56×10^6), we obtain a cumulative noise count lasting for 1 s, that is, noise counting rate N . There is no change in noise counting rate with or without 795 nm input pulse, which means that the noise at 795 nm is completely filtered out.

Next, we study the suppression of pump induced noise by the three-stage filtering system in detail. The input light at 795 nm is blocked, and only the pumping light at 1560 nm is injected into the waveguide module. In order to avoid missing counts due to the long dead time of SPD, the injected pumping light is in the form of pulses with period of 25 μ s and duration of 1 μ s. We measure the noise counts when the light is on. Figure 3 shows the noise counting rate N as a function of the pumping power P_p under different filtering conditions. P_p is the pumping power coupled into the 2×1 combiner.

Initially, the two etalons and F-P cavity in the three-stage filtering system are bypassed, leaving only the first-stage filter. The measured noise is shown by the blue triangles (data points on the top) in Figure 3. From the data we can see that after the first-stage filter, the noise generated by the pumping light remains at a fairly high level, such as $N = 1.36 \times 10^6$ /s for $P_p = 350$ mW. Then, the second-stage filter is added in the filtering system, and the measured noise level is significantly reduced, shown by the red circles

(data points in the middle). Finally, the third stage filter is also added, and the noise is further reduced as shown by the black squares (data points in the bottom). Under this condition, for $P_p = 350$ mW the noise counting rate is decreased to $N = 780$ /s. The noise level is related to the pumping power. We fit the noise data by using the expression [29]: $N(P_p) = \alpha \times P_p + DC$, where α is the linear coefficient, and $DC = 2.5 \times 10^2$ /s is the dark count rate of SPD. The solid lines in Figure 3 are the fitted curves, which are in good agreement with the experimental data. For the fitted lines from top to bottom, the slope α is taken as 4.5×10^3 /mW/s, 4.5×10 /mW/s and 1.52 /mW/s, respectively. It is illustrated that the second-stage filter (cascaded etalons) reduces the noise level by two orders of magnitude, and the third-stage filter (F-P cavity) reduces the noise by another order of magnitude.

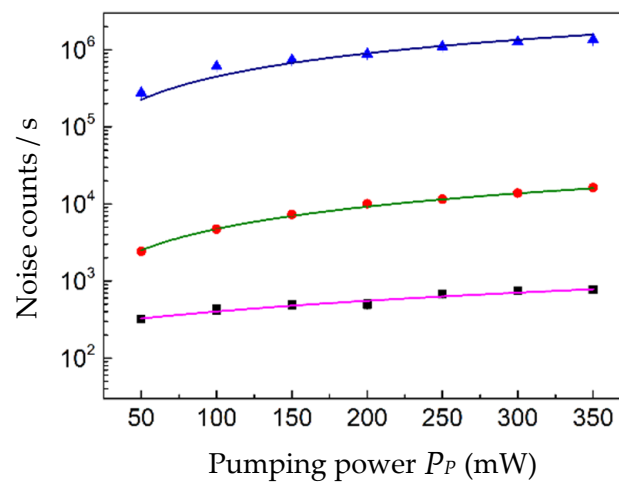


Figure 3. Noise counting rate as a function of the pumping power under different filtering conditions. When the etalons and F-P cavity are bypassed, only the first-stage filter is remained, the noise level is shown by the blue triangles. The red circles show the noise level when the second-stage filter is added into the filtering system. The black squares represent the noise level when the third-stage filter is further added. The solid lines are corresponding fitting curves.

The pump-induced noise includes the leakage of pump light at 1560 nm, SRS noise, and the SHG of strong pump at 780 nm. In order to assess the noise level at 1560 nm and 780 nm, we put another band-pass filter centered at 1621 nm behind the filtering system, which filters out most of the noise at 1560 nm and 780 nm, and remaining SRS around 1621 nm. For $P_p = 350$ mW, the measured noise count rate is 620/s. The addition of 1621 nm bandpass filter did not significantly reduce the noise count. The reduction in noise count is due to the transmittance loss of the inserted filter itself. This indicates that the noise at 1560 nm and 780 nm has been filtered out by the original filtering system, and the noise is mainly SRS after the filtering system.

We study the influence of the filtering system on the shape of the converted pulse for different input pulse widths. Here the input pulse is taken as Gaussian shape with $\mu_{in} = 50$. The full width at half maximum (FWHM) of the input pulse is $\Delta t_{in} = 53$ ns, 112 ns and 182 ns in Figure 4a,b,c, respectively. We use SPD to measure the converted light field after the filtering system, and accumulate the measurement results by FPGA to acquire the photon statistics distributions of the converted pulse, as shown by the gray histogram in Figure 4. The sampling accuracy of FPGA is 10 ns. By fitting the photon distribution with Gaussian function, the pulse shape of the converted field after the filtering system is obtained, as shown by the red solid lines in Figure 4. For $\Delta t_{in} = 53$ ns, 112 ns and 182 ns, the FWHM of the fitted Gauss distributions are $\Delta t_{out} = 102$ ns, $\Delta t_{out} = 133$ ns and $\Delta t_{out} = 190$ ns, respectively. We can see that the input pulse will be significantly broadened when its FWHM is less than 100 ns. So the tolerable narrowest bandwidth of the filtering system depends on the duration of the pulse to be filtered. When the frequency conversion

is used as a quantum interface to connect quantum storage and fiber-based communication, one needs to choose proper bandwidth of the filtering system according to the pulse width of light field emitted from the storage medium, so as to ensure the converted pulse passes through without distortion and the noise is filtered to the greatest extent.

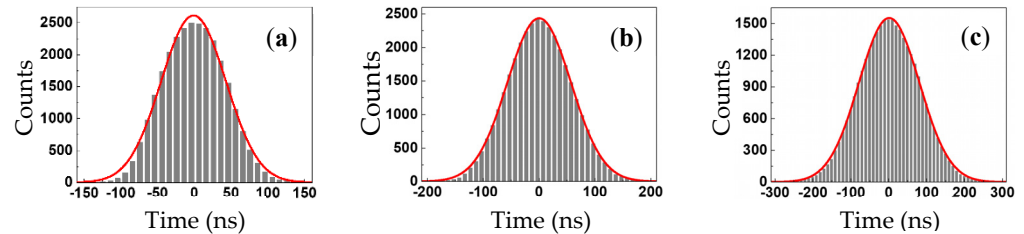


Figure 4. The influence of the three-stage filtering system on the temporal shape of converted pulse. The gray columns are the photon statistics distributions of the converted fields measured by SPD with input FWHM of Δt_{in} . Red solid lines are the fitted Gauss distributions with FWHM of Δt_{out} . (a) $\Delta t_{in} = 53$ ns, $\Delta t_{out} = 102$ ns. (b) $\Delta t_{in} = 112$ ns, $\Delta t_{out} = 133$ ns. (c) $\Delta t_{in} = 182$ ns, $\Delta t_{out} = 190$ ns. The pumping power is 350 mW. The counts is the accumulation of 5×10^5 repeated measurements.

4. Conversion Device Characterization

On the basis of the strong noise filtering, we study the characteristics of the frequency conversion devices. Firstly, we measured the detection probability of the converted pulse D_s in terms of the pumping power P_p , shown by the blue squares in Figure 5a. Here, the average photon number contained in the input pulse is $\mu_{in} = 5$. The temporal FWHM of the 795 nm input pulse is taken as 100 ns, and the measuring window width is 400 ns. The pink circles in Figure 5a show the noise detection probability D_n when only the pumping beam is injected. The red triangles represent the net signal detection probability $D_s - D_n$. Limited by the maximum allowable power of fiber end face, the maximum pumping power coupled into the 2×1 combiner P_p is 350 mW. The signal (noise) detection probability D_s (D_n) increases almost linearly with the pumping power within the current power range of the pumping light. The net signal $D_s - D_n$ is close to D_s due to the extremely low noise level even at $P_p = 350$ mW ($D_s = 0.57\%$, $D_n = 0.028\%$).

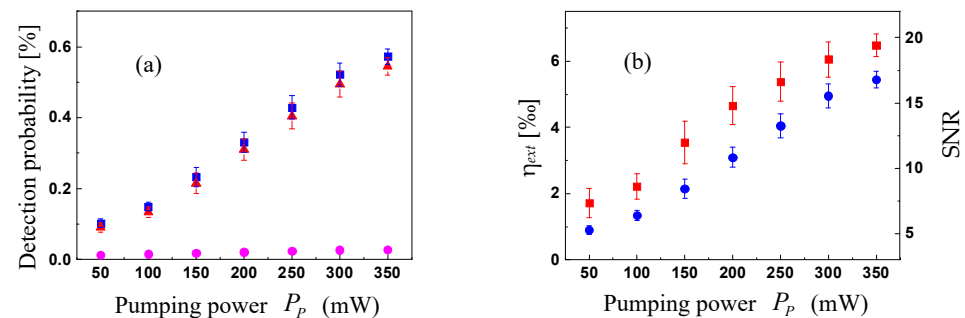


Figure 5. (a) Detection probability with (D_s , blue squares) and without (D_n , pink circles) input signal ($\mu_{in} = 5$) as a function of the pumping power P_p . The red triangles are the net signal ($D_s - D_n$). (b) The SNR of the converted field after the filtering system as a function of the pumping power P_p (red squares, right axis). The external device conversion efficiency η_{ext} is shown by the blue circles on the left axis.

The total conversion efficiency including all losses can be calculated by $\eta_{tot} = (D_s - D_n)/\mu_{in}$, and $\eta_{tot}^{max} = 1.08 \times 10^{-3}$ at $P_p = 350$ mW. By correcting for the quantum efficiency of SPD (20%), the maximum external device conversion efficiency $\eta_{ext}^{max} = 0.54\%$, which can be interpreted as the probability to find a photon at the output of the converted device (including the filtering system) with $\mu_{in} = 1$. Next, by further correcting for the transmission of the filtering system (11%), we calculate the conversion efficiency of the fiber-coupled PPLN waveguide module ($\eta_{wg}^{max} = 4.9\%$), corresponding to μ_{out}/μ_{in} , where

μ_{out} is the average photon number of the converted pulse at the output of the conversion module. Finally, it can be deduced that the maximum conversion efficiency inside the waveguide $\eta_{int}^{max} = 20.4\%$, by considering the transmission efficiency of the 2×1 combiner (0.67), the input coupling efficiency of the waveguide (0.55), and the output coupling efficiency of waveguide (0.65).

According to $SNR = (D_s - D_n)/D_n$, we calculate the SNR of the converted pulse ($\mu_{in} = 5$) after the filtering system, shown in Figure 5b. The SNR increases with the pumping power in the current power range of the pumping light, and the SNR achieves 19.4 at $P_p = 350$ mW. From Figure 5b we can see that SNR and the external device conversion efficiency have the same growth trend as the pumping power increases due to low noise level. In general, the pumping power at the optimal SNR is much lower than that at the maximum conversion efficiency [23,29]. The reduction in noise level is beneficial to the simultaneous optimization of SNR and conversion efficiency.

The application of the fiber-coupled waveguide module limits the efficiency of the conversion device. On one hand, the insertion loss of the 2×1 combiner and the coupling loss of the waveguide module to output fiber are introduced compared to a free-space coupled PPLN waveguide. On the other hand, the pumping power is limited by the maximum allowable power of the fiber end face (500 mW). The maximum pumping power coupled into the 2×1 combiner is 350 mW due to the coupling efficiency of the input fiber of the 2×1 combiner (0.7). The corresponding maximum pumping power entering the waveguide is only 117 mW, due to the transmission of the 2×1 combiner (0.61) and the input coupling efficiency of the waveguide (0.55). In the case of free-space coupled waveguide, the internal conversion efficiency can be further improved by increasing the pumping power.

The SNR of the converted pulse is also related to the duration of the input pulse. For a pulse of long duration, a large measurement window is needed to obtain its complete information, which means that more noise is included in the measurement process and the SNR of converted pulse is decreased. The noise level of the converted pulse with different durations can be represented by parameter μ_1 , which is the photon number contained in the input pulse to make the SNR of converted pulse equal to 1. We measure μ_1 as a function of the temporal FWHM of input pulse Δt_{in} , as shown in Figure 6. The measurement window is taken to be three times the temporal FWHM of the output pulse after filtering system, in which more than 99% of the converted pulse can be included. Although the external device conversion efficiency is low ($\eta_{ext} = 0.51\%$), the value of μ_1 is less than 1 for $\Delta t_{in} = 250$ ns, which benefits from strong noise suppression. The solid line in Figure 6 is a linear fitting with no offset for the experimental data. Except for $\Delta t_{in} = 50$ ns, the other data points are in good agreement with the linear fitting. The reason is that the temporal FWHM of output pulse is broadened twice when $\Delta t_{in} = 50$ ns, while the output pulse width of other data points is close to that of the input pulse.

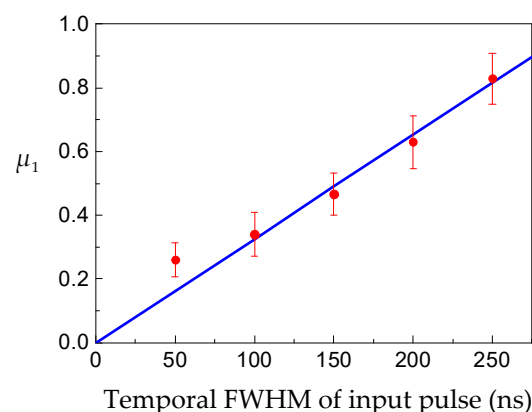


Figure 6. The mean number of photons in the input pulse to achieve SNR = 1 (μ_1) as a function of the FWHM of input pulse. The pumping power is 315 mW. The solid line is a linear fitting with no offset.

5. Conclusions and Discussion

We demonstrate the frequency conversion interface from rubidium D1 line to communication L-band by using DFG process in PPLN waveguide. In order to suppress broadband SRS noise produced by the pumping field, we design a hierarchical filtering system to narrow the noise bandwidth to 11.7 MHz. To our knowledge, this is the narrowest filtering bandwidth applied in frequency down conversion. The filtering system includes a band-pass filter, an FBG, two cascaded etalons and a confocal F-P cavity with low finesse. These optical components are easy to use, so the filtering method is suitable to be popularized in the experimental research of frequency conversion.

We study the influence of the filtering system on the output pulse shape, and find that the shape of input Gaussian pulse can be preserved when its temporal FWHM is not less than 100 ns. Benefiting from the strong noise suppression, even at such low external device conversion efficiency (0.51%) and large duration ($\Delta t_{in} = 250$ ns) of the input pulse, the average photon number contained in the input pulse $\mu_1 < 1$ to require the SNR of converted pulse equal to 1. At present, using bridge PPLN waveguide, the external conversion efficiency of DFG can reach more than 30% [15,23,28]. If our filtering system is combined with such an efficient bridge waveguide, it is predicted that the SNR of the converted pulse with $\Delta t_{in} = 100$ ns and $\mu_{in} = 1$ will exceed 20, which can be used as the frequency conversion interface in fiber quantum networks.

At present, the transmittance of our filtering system is only 11%. The low transmittance will reduce the rate of entanglement distribution in quantum network. We propose a scheme to improve the performance of the filtering system. If we add two additional etalons with length of 5.4 mm and 7.5 mm (finesse of 30) to the filtering system, the noise suppression range of the cascaded four etalons is extended to 2000 GHz (17 nm). In this way, the Bragg fiber grating can be removed in the filtering system. Thus, the filtering system consists of four etalons, an F-P cavity, two DMs and two band-pass filters. It is not difficult to optimize the single etalon efficiency to 95% and the F-P cavity efficiency to 90%. By choosing DMs and band-pass filters with high transmittance (>99%), the overall throughput of the filtering system can reach 70%.

By using the frequency conversion interface, we calculate the needed time for entanglement establishment between two remote quantum nodes based on DLCZ (for Duan, Lukin, Cirac, and Zoller) quantum repeater scheme [4]. In the scheme the success probability for entanglement generation is expressed as $P_0 = (\chi^2 e^{-L_0/L_{att}} \eta_{FC}^2 \eta_{TD}^2) / 2$, where χ is the excitation probability of Stokes photon, L_0 is the distance between the two nodes, L_{att} is the attenuation length of the fiber channel, η_{FC} is the efficiency of frequency conversion module, and η_{TD} is the total detection efficiency. The needed time for a single entanglement generation attempt is $T_0 = T_{cc} / P_0$, where $T_{cc} = L_0 / c$ is the communication time interval and c is the light speed in fiber. Combining a frequency conversion module with an efficiency of 30% and a narrow-band filter system with an efficiency of 70% to form a quantum frequency conversion interface, the whole efficiency of the interface is 21%. When such an interface is used for quantum repeater, the photon at L-band is used for remote transmission and the transmission loss in fiber is ~0.18 dB/km. The needed time for entanglement generation between two quantum nodes 50 km apart is 38 s with $\chi = 3.8\%$, $\eta_{FC} = 30\%$, and $\eta_{TD} = 90\%$. If a photon at 795 nm is directly transmitted over a long distance without frequency conversion interface (transmission loss ~4 dB/km), the time required to establish entanglement is 4.3×10^{19} s with same L_0 , χ and η_{TD} . From the above analysis, it can be concluded that the frequency conversion interface has the potential ability to greatly improve the performance of quantum repeater.

Author Contributions: Conceptualization, S.L. and H.W.; investigation, S.L., L.C. and H.W.; data curation, S.L., J.B. and Q.D.; writing—original draft preparation, L.C. and S.L.; writing—review and editing, S.L.; supervision, H.W.; funding acquisition, H.W. All authors have read and agreed to the published version of the manuscript.

Funding: This research was funded by Key Project of the Ministry of Science and Technology of China (Grant No. 2016YFA0301402), National Natural Science Foundation of China (Grants: No. 11834010, 12174235, and 61805133), Shanxi “1331 Project” Key Subjects Construction.

Conflicts of Interest: The authors declare no conflict of interest.

References

1. Gisin, N.; Thew, R. Quantum communication. *Nat. Photonics* **2007**, *1*, 165–171. [\[CrossRef\]](#)
2. Wehner, S.; Elkouss, D.; Hanson, R. Quantum internet: A vision for the road ahead. *Science* **2018**, *362*, 303. [\[CrossRef\]](#) [\[PubMed\]](#)
3. Briegel, H.-J.; Dür, W.; Cirac, J.I.; Zoller, P. Quantum Repeaters: The Role of Imperfect Local Operations in Quantum Communication. *Phys. Rev. Lett.* **1998**, *81*, 5932–5935. [\[CrossRef\]](#)
4. Sangouard, N.; Simon, C.; de Riedmatten, H.; Gisin, N. Quantum repeaters based on atomic ensembles and linear optics. *Rev. Mod. Phys.* **2011**, *83*, 33–80. [\[CrossRef\]](#)
5. Van Loock, P.; Alt, W.; Becher, C.; Benson, O.; Boche, H.; Deppe, C.; Eschner, J.; Höfling, S.; Meschede, D.; Michler, P.; et al. Extending Quantum Links: Modules for Fiber- and Memory-Based Quantum Repeaters. *Adv. Quantum Technol.* **2020**, *3*, 1900141. [\[CrossRef\]](#)
6. Heller, L.; Farrera, P.; Heinze, G.; de Riedmatten, H. Cold-Atom Temporally Multiplexed Quantum Memory with Cavity-Enhanced Noise Suppression. *Phys. Rev. Lett.* **2020**, *124*, 210504. [\[CrossRef\]](#) [\[PubMed\]](#)
7. Cao, M.-T.; Hoffet, F.; Qiu, S.-W.; Sheremet, A.S.; Laurat, J. Efficient reversible entanglement transfer between light and quantum memories. *Optica* **2020**, *7*, 1440–1444. [\[CrossRef\]](#)
8. Hofmann, J.; Krug, M.; Ortegel, N.; Gérard, L.; Weber, M.; Rosenfeld, W.; Weinfurter, H. Heralded Entanglement Between Widely Separated Atoms. *Science* **2012**, *337*, 72–75. [\[CrossRef\]](#)
9. Specht, H.P.; Nölleke, C.; Reiserer, A.; Uphoff, M.; Figueroa, E.; Ritter, S.; Rempe, G. A single-atom quantum memory. *Nature* **2011**, *473*, 190–193. [\[CrossRef\]](#)
10. Duan, L.-M.; Monroe, C. Colloquium: Quantum networks with trapped ions. *Rev. Mod. Phys.* **2010**, *82*, 1209–1224. [\[CrossRef\]](#)
11. Wang, P.-F.; Luan, C.-Y.; Qiao, M.; Um, M.; Zhang, J.-H.; Wang, Y.; Yuan, X.; Gu, M.; Zhang, J.-N.; Kim, K. Single ion qubit with estimated coherence time exceeding one hour. *Nat. Commun.* **2021**, *12*, 233. [\[CrossRef\]](#) [\[PubMed\]](#)
12. He, Y.; He, Y.-M.; Wei, Y.-J.; Jiang, X.; Chen, M.-C.; Xiong, F.-L.; Zhao, Y.; Schneider, C.; Kamp, M.; Höfling, S.; et al. Indistinguishable Tunable Single Photons Emitted by Spin-Flip Raman Transitions in InGaAs Quantum Dots. *Phys. Rev. Lett.* **2013**, *111*, 237403. [\[CrossRef\]](#) [\[PubMed\]](#)
13. Tchegbotareva, A.; Hermans, S.L.N.; Humphreys, P.C.; Voigt, D.; Harmsma, P.J.; Cheng, L.K.; Verlaan, A.L.; Dijkhuizen, N.; de Jong, W.; Dréau, A.; et al. Entanglement between a Diamond Spin Qubit and a Photonic Time-Bin Qubit at Telecom Wavelength. *Phys. Rev. Lett.* **2019**, *123*, 063601. [\[CrossRef\]](#) [\[PubMed\]](#)
14. Radnaev, A.G.; Dudin, Y.O.; Zhao, R.; Jen, H.H.; Jenkins, S.D.; Kuzmich, A.; Kennedy, T.A.B. A quantum memory with telecom-wavelength conversion. *Nat. Phys.* **2010**, *6*, 894–899. [\[CrossRef\]](#)
15. Van Leent, T.; Bock, M.; Garthoff, R.; Redeker, K.; Zhang, W.; Bauer, T.; Rosenfeld, W.; Becher, C.; Weinfurter, H. Long-Distance Distribution of Atom-Photon Entanglement at Telecom Wavelength. *Phys. Rev. Lett.* **2020**, *124*, 010510. [\[CrossRef\]](#)
16. Greve, K.D.; Yu, L.; McMahon, P.L.; Pelc, J.S.; Natarajan, C.M.; Kim, N.Y.; Abe, E.; Maier, S.; Schneider, C.; Kamp, M.; et al. Quantum-dot spin-photon entanglement via frequency downconversion to telecom wavelength. *Nature* **2012**, *491*, 421–425. [\[CrossRef\]](#)
17. Chang, W.; Li, C.; Wu, Y.-K.; Jiang, N.; Zhang, S.; Pu, Y.-F.; Chang, X.-Y.; Duan, L.-M. Long-distance entanglement between a multiplexed quantum memory and a telecom photon. *Phys. Rev. X* **2019**, *9*, 041033. [\[CrossRef\]](#)
18. Afzelius, M.; Gisin, N.; de Riedmatten, H. Quantum memory for photons. *Phys. Today* **2015**, *68*, 42–47. [\[CrossRef\]](#)
19. Maring, N.; Farrera, P.; Kutluer, K.; Mazzera, M.; Heinze, G.; de Riedmatten, H. Photonic quantum state transfer between a cold atomic gas and a crystal. *Nature* **2017**, *551*, 485–488. [\[CrossRef\]](#)
20. Takesue, H. Single-photon frequency down-conversion experiment. *Phys. Rev. A* **2010**, *82*, 013833. [\[CrossRef\]](#)
21. Ding, Y.; Ou, Z.Y. Frequency downconversion for a quantum network. *Opt. Lett.* **2010**, *35*, 2591–2593. [\[CrossRef\]](#) [\[PubMed\]](#)
22. Maring, N.; Lago-Rivera, D.; Lenhard, A.; Heinze, G.; de Riedmatten, H. Quantum frequency conversion of memory-compatible single photons from 606 nm to the telecom C-band. *Optica* **2018**, *5*, 507–513. [\[CrossRef\]](#)
23. Zaske, S.; Lenhard, A.; Becher, C. Efficient frequency downconversion at the single photon level from the red spectral range to the telecommunications C-band. *Opt. Express* **2011**, *19*, 12825–12836. [\[CrossRef\]](#) [\[PubMed\]](#)
24. Strassmann, P.C.; Martin, A.; Gisin, N.; Afzelius, M. Spectral noise in frequency conversion from the visible to the telecommunication C-band. *Opt. Express* **2019**, *27*, 14298–14307. [\[CrossRef\]](#) [\[PubMed\]](#)
25. Duan, L.-M.; Lukin, M.D.; Cirac, J.I.; Zoller, P. Long-distance quantum communication with atomic ensembles and linear optics. *Nature* **2001**, *414*, 413–418. [\[CrossRef\]](#)
26. Yuan, Z.-S.; Chen, Y.-A.; Zhao, B.; Chen, S.; Schmiedmayer, J.; Pan, J.-W. Experimental demonstration of a BDCZ quantum repeater node. *Nature* **2008**, *454*, 1098–1101. [\[CrossRef\]](#)
27. Olmschenk, S.; Matsukevich, D.N.; Maunz, P.; Hayes, D.; Duan, L.-M.; Monroe, C. Quantum Teleportation Between Distant Matter Qubits. *Science* **2009**, *323*, 486–489. [\[CrossRef\]](#)

28. Yu, Y.; Ma, F.; Luo, X.-Y.; Jing, B.; Sun, P.-F.; Fang, R.-Z.; Yang, C.-W.; Liu, H.; Zheng, M.-Y.; Xie, X.-P.; et al. Entanglement of two quantum memories via fibres over dozens of kilometres. *Nature* **2020**, *578*, 240–245. [[CrossRef](#)]
29. Fernandez-Gonzalvo, X.; Corrielli, G.; Albrecht, B.; Grimaud, M.I.; Cristiani, M.; de Riedmatten, H. Quantum frequency conversion of quantum memory compatible photons to telecommunication wavelengths. *Opt. Express* **2013**, *21*, 19473–19487. [[CrossRef](#)]
30. Bock, M.; Eich, P.; Kucera, S.; Kreis, M.; Lenhard, A.; Becher, C.; Eschner, J. High-fidelity entanglement between a trapped ion and a telecom photon via quantum frequency conversion. *Nat. Commun.* **2018**, *9*, 1998. [[CrossRef](#)]
31. Walker, T.; Miyaniishi, K.; Ikuta, R.; Takahashi, H.; Kashanian, S.V.; Tsujimoto, Y.; Hayasaka, K.; Yamamoto, T.; Imoto, N.; Keller, M. Long-Distance Single Photon Transmission from a Trapped Ion via Quantum Frequency Conversion. *Phys. Rev. Lett.* **2018**, *120*, 203601. [[CrossRef](#)] [[PubMed](#)]
32. Dréau, A.; Tchegbotareva, A.; Mahdaoui, A.E.; Bonato, C.; Hanson, R. Quantum Frequency Conversion of Single Photons from a Nitrogen-Vacancy Center in Diamond to Telecommunication Wavelengths. *Phys. Rev. Appl.* **2018**, *9*, 064031. [[CrossRef](#)]
33. Ikuta, R.; Kobayashi, T.; Yasui, S.; Miki, S.; Yamashita, T.; Terai, H.; Fujiwara, M.; Yamamoto, T.; Koashi, M.; Sasaki, M.; et al. Frequency down-conversion of 637 nm light to the telecommunication band for non-classical light emitted from NV centers in diamond. *Opt. Express* **2014**, *22*, 11205–11214. [[CrossRef](#)] [[PubMed](#)]
34. Wang, X.-J.; Yang, S.-J.; Sun, P.-F.; Jing, B.; Li, J.; Zhou, M.-T.; Bao, X.-H.; Pan, J.-W. Cavity-Enhanced Atom-Photon Entanglement with Subsecond Lifetime. *Phys. Rev. Lett.* **2021**, *126*, 090501. [[CrossRef](#)] [[PubMed](#)]
35. Tian, L.; Xu, Z.-X.; Chen, L.-R.; Ge, W.; Yuan, H.-X.; Wen, Y.-F.; Wang, S.-Z.; Li, S.-J.; Wang, H. Spatial Multiplexing of Atom-Photon Entanglement Sources using Feedforward Control and Switching Networks. *Phys. Rev. Lett.* **2017**, *119*, 130505. [[CrossRef](#)]
36. Li, C.; Jiang, N.; Wu, Y.-K.; Chang, W.; Pu, Y.-F.; Zhang, S.; Duan, L.-M. Quantum Communication between Multiplexed Atomic Quantum Memories. *Phys. Rev. Lett.* **2020**, *124*, 240504. [[CrossRef](#)]
37. Lobino, M.; Kupchak, C.; Figueroa, E.; Lvovsky, A.I. Memory for Light as a Quantum Process. *Phys. Rev. Lett.* **2009**, *102*, 203601. [[CrossRef](#)]
38. Dudin, Y.O.; Jenkins, S.D.; Zhao, R.; Matsukevich, D.N.; Kuzmich, A.; Kennedy, T.A.B. Entanglement of a Photon and an Optical Lattice Spin Wave. *Phys. Rev. Lett.* **2009**, *103*, 020505. [[CrossRef](#)]
39. Zhao, B.; Chen, Z.B.; Chen, Y.A.; Schmiedmayer, J.; Pan, J.W. Robust Creation of Entanglement between Remote Memory Qubits. *Phys. Rev. Lett.* **2007**, *98*, 240502. [[CrossRef](#)]
40. Yamamoto, Y.; Kawaguchi, Y.; Hirano, M. Low-Loss and Low-Nonlinearity Pure-Silica-Core Fiber for C- and L-band Broadband Transmission. *J. Lightw. Technol.* **2016**, *34*, 321–326. [[CrossRef](#)]
41. Richardson, D.J.; Fini, J.M.; Nelson, L.E. Space-division multiplexing in optical fibres. *Nat. Photonics* **2013**, *7*, 354–362. [[CrossRef](#)]
42. Kuo, P.S.; Pelc, J.S.; Slattery, O.; Kim, Y.-S.; Fejer, M.M.; Tang, X. Reducing noise in single-photon-level frequency conversion. *Opt. Lett.* **2013**, *38*, 1310–1312. [[CrossRef](#)] [[PubMed](#)]
43. Farrera, P.; Maring, N.; Albrecht, B.; Heinze, G.; de Riedmatten, H. Nonclassical correlations between a C-band telecom photon and a stored spin-wave. *Optica* **2016**, *3*, 1019–1024. [[CrossRef](#)]
44. Ikuta, R.; Kobayashi, T.; Kawakami, T.; Miki, S.; Yabuno, M.; Yamashita, T.; Terai, H.; Koashi, M.; Mukai, T.; Yamamoto, T.; et al. Polarization insensitive frequency conversion for an atom-photon entanglement distribution via a telecom network. *Nat. Commun.* **2018**, *9*, 1997. [[CrossRef](#)]
45. Drever, R.W.P.; Hall, J.L.; Kowalski, F.V.; Hough, J.; Ford, G.M.; Munley, A.J.; Ward, H. Laser phase and frequency stabilization using an optical resonator. *Appl. Phys. B* **1983**, *31*, 97–105. [[CrossRef](#)]